Upwind residual distribution for shallow-water ocean modelling

D. Sármány[a,*], M.E. Hubbard[a]

[a] *School of Computing, University of Leeds, LS2 9JT, Leeds, United Kingdom*

Abstract

This article describes residual distribution for the rotating shallow water equations arising in oceanographic and meteorological modelling. The method is similar to (dis)continuous finite elements in that it is well suited for unstructured, locally refined meshes – therefore promising to be a viable alternative to more traditional methods for shallow-water ocean modelling. It has, however, two main advantages over finite-element methods. First, it creates a framework in which nonlinear dynamics can be represented very naturally. Second, by combining the treatment of the flux and source terms, it makes the preservation of certain balance properties – especially hydrostatic balance – easier to guarantee. The methods considered in this article have been previously shown to preserve many of the important physical properties of the original equations, such as conservation, oscillation-free behaviour and the exact preservation of hydrostatic balance. This work is intended as the first step into investigating the method's suitability for modelling geophysical fluids. This is done through a number of carefully-chosen test cases, which include both f_0-plane and β-plane approximations as well as non-flat bottom topography.

Keywords: upwind residual distribution, rotating shallow-water equations, discontinuous representation in time, balance properties for hyperbolic equations

1. Introduction

There has been considerable research interest in the past two decades in numerical methods for ocean modelling that are suitable for unstructured triangular meshes. It is primarily because these meshes can both resolve complex geometric features (such as coastal regions) and use dynamical local mesh adaptation to reduce computational costs. The most established of these are finite-element (FE) methods, see Ford et al. (2004a,b), Maddison et al. (2011), and finite-volume (FV) methods, see Fringer et al. (2006), Audusse et al. (2004), Bouchut (2007). More recently, however, high-order spectral element (SE) methods, see Ma (1993), Iskandarani et al. (2003), Giraldo and Taylor (2006), and discontinuous Galerkin (DG) methods, see Eskilsson and Sherwin (2004), Giraldo and Warburton (2008), Cotter et al. (2009), have also been of interest thanks to their high accuracy in resolving linear and weakly nonlinear waves.

In this work, we offer an alternative formulation in the framework of residual distribution (RD). It was first introduced in Roe (1982), in which it was called fluctuation

*Corresponding author. Tel.: +44 113 343 4697. Fax: +44 113 343 5457.

Email addresses: d.sarmany@leeds.ac.uk (D. Sármány), m.e.hubbard@leeds.ac.uk (M.E. Hubbard)

splitting, as a more accurate alternative to flux-based FV methods for the numerical discretisation of hyperbolic conservation laws. It has, indeed, been proved very successful in two-dimensional steady-state problems thanks to its ability to better represent the physical properties of the underlying partial differential equations, see Deconinck et al. (1993). In particular, it can naturally be constructed to be upwind, positive and conservative while remaining second-order accurate when the discrete representation is linear. Recent reviews of the field can be found in Deconinck and Ricchiuto (2007) and Abgrall (2012).

Extending the RD framework to time-dependent problems, however, is far from straightforward and is a field of active research. For the nonlinear shallow-water equations, a number of formulations have been designed in Ricchiuto et al. (2007), Ricchiuto and Bollermann (2009), Ricchiuto (2011a) and Sármány et al. (2012). While these schemes often lack rigorous mathematical proofs for the preservation of positivity, they typically nonetheless exhibit oscillation-free behaviour numerically. In Hubbard and Ricchiuto (2011) and Sármány et al. (2012), in particular, the space-time approach of Csík and Deconinck (2002) was reformulated so that the discrete representation in time is allowed to be discontinuous. This removes the time-step restriction on time marching and gives rise to an unconditionally stable and positive implicit scheme. It was tested in Sármány et al. (2012) on a number of test cases and the results were rather promising.

The RD framework also provides a simple formulation to include source terms in the residual. Most recent research has been focusing on the treatment of non-flat bottom topography, also called bathymetry, and exact preservation of hydrostatic balance thereover, see Ricchiuto et al. (2007), Ricchiuto and Bollermann (2009) and Sármány et al. (2012). In Ricchiuto (2011b), in particular, a case is made that, for a positive scheme on unstructured meshes, hydrostatic balance is more naturally preserved in the RD framework than in either finite volumes or finite elements (see **?** and references therein).

This work extends the treatment of source terms to the Coriolis force, essentially discretising the rotating shallow-water equations. The presented formulation does not preserve the geostrophic balance exactly. Nevertheless, in many time-dependent situations the geostrophic balance is sufficiently well represented for the numerical discretisation not to produce ostensible spurious effects. The main difficulty for preserving the geostrophic balance exactly for the FE method on unstructured triangular meshes is that it involves some kind of mixed formulation similar to Cotter et al. (2009). This, in turn, often introduces spurious inertial oscillations because the number of discrete (vector-valued) momentum equations does not equal the number of discrete (scalar-valued) mass equations, as shown in **?** and **?**. In the finite-volume framework, it is only recently that the preservation of geostrophic balance has been addressed in **?** – but only on structured rectangular meshes. Upwind RD offers at least two favourable properties in this respect. First, it is genuinely upwind (i.e. no information is sent downstream) so it does not produce spurious pressure oscillations. Second, it is unstaggered on unstructured triangular meshes so it has the same number of (scalar-valued) mass and (vector-valued) momentum equations and, therefore, does not suffer from spurious inertial oscillations. These two properties, however, do not necessarily suggest that RD is completely free of spurious (or computational) modes. In order to assess the spectral properties of the scheme, a Fourier analysis needs to be carried out on a shallow-water system that is linearised around the conservative variables. This is currently ongoing work and will be reported elsewhere.

In addition to the Coriolis force, this work also includes wind force and bottom friction in the source term to be able to simulate ocean circulation with nonlinear effects. The remaining part of this article is organised as follows. Section 2 gives a short description of the oceanic shallow-water equations so that the source term includes bottom topography, Coriolis force, wind force and bottom friction. Section 3 introduces the concept of residual distribution for steady-state problems, Section 4 describes the space-time scheme with discontinuous representation in time, and Section 5 addresses the most important implementation aspects. In Section 6, the schemes are tested on four important examples, three of which are time-dependent. Finally, conclusions and outlook are provided in Section 7.

2. The rotating shallow-water equations

In this article, we apply the RD framework to the frictionless rotating shallow-water equations with possibly non-flat bottom topography. Thus we seek the solution to the system

$$\partial_t U + \nabla \cdot \boldsymbol{F}(U) + S(U) = 0 \tag{1}$$

with

$$\begin{aligned} U &= \begin{bmatrix} d \\ du \\ dv \end{bmatrix}, \quad \boldsymbol{F} = \begin{bmatrix} F_x & F_y \end{bmatrix} = \begin{bmatrix} du & dv \\ du^2 + \frac{gd^2}{2} & duv \\ duv & dv^2 + \frac{gd^2}{2} \end{bmatrix}, \\ S &= \begin{bmatrix} 0 \\ gd\frac{\partial b(x,y)}{\partial x} - fdv - \frac{\tau_x}{\rho} + \gamma du \\ gd\frac{\partial b(x,y)}{\partial y} + fdu - \frac{\tau_y}{\rho} + \gamma dv \end{bmatrix}, \end{aligned} \tag{2}$$

and with suitable initial and boundary conditions. Here, d is the water height, $\boldsymbol{u} = [u, v]^T$ is the velocity field, b is the height of the bottom topography, $\eta = d + b$ is the level of the free surface, $\boldsymbol{\tau} = [\tau_x, \tau_y]^T$ is the wind stress, ρ is the density of water, and γ is the bottom friction. The Coriolis parameter is approximated as $f = f_0 + \beta y$. With $\beta = 0$ this is the constant f_0-plane approximation, which is suitable for describing mid-latitude processes. The β-plane approximation ($\beta \neq 0$) is typically needed in regions nearer the equator.

For numerical computations without wind stress and bottom friction (i.e. $\boldsymbol{\tau} = \boldsymbol{0}$ and $\gamma = 0$), we solve the non-dimensional version of (1). This is derived through the substitutions

$$t = Tt', \quad (x, y) = L(x', y'), \quad d = Hd', \quad b = Hb', \quad (u, v) = W(u', v'), \quad f' = f/T, \tag{3}$$

where T, L, H and W are the characteristic time, length, height and velocity in physical dimensions. Dropping the primes we formally get (1) with $g = 1$ and $f \to fT$.

In the following two sections, we describe both steady-state and space-time RD schemes for the oceanic shallow water system (1)–(2). In the latter case, we use discontinuous representation in time, as in Hubbard and Ricchiuto (2011) and Sármány et al. (2012), to eliminate the time-step constraint (given in Csík and Deconinck (2002)) associated with the time-marching procedure.

2.1. Notation

Throughout the article, we assume a two-dimensional spatial domain $\Omega \subset \mathbb{R}^2$, which is tessellated into a set of triangles, so that $\Omega \approx \Omega_h = \cup_{E \in \Omega_h} E$, where E denotes a given triangle. Let $D_i = \cup_{i \in E} E$ denote the set of triangles connected to node i. Finally, for the time-dependent simulations, we define the space-time prism E_t over the triangle E as $E_t = E \times [t^n, t^{n+1}]$, where t^n and t^{n+1} are the bottom and top time levels of the prism.

3. Steady-state residual distribution

Consider the system (1) in the steady-state limit,

$$\nabla \cdot \boldsymbol{F}(U) + S(U) = 0 \qquad \text{or} \qquad \boldsymbol{\mathcal{A}}(U) \cdot \nabla U + S(U) = 0, \tag{4}$$

with appropriate boundary conditions. Here, $\boldsymbol{F}(U)$ represents the flux Jacobian and $\boldsymbol{\mathcal{A}}(U) = [\mathcal{A}_x, \mathcal{A}_y] = [\partial F_x/\partial U, \partial F_y/\partial U] = \partial \boldsymbol{F}/\partial U$ is the wave-speed tensor. The steady-state elementwise residual is then given as

$$\Phi_E = \int_E (\nabla \cdot \boldsymbol{F}(U) + S(U)) \, \mathrm{d}x \, \mathrm{d}y \tag{5}$$

so that

$$\Phi = \int_{\Omega_h} (\nabla \cdot \boldsymbol{F}(U) + S(U)) \, \mathrm{d}x \, \mathrm{d}y = \sum_{E \in \Omega_h} \Phi_E.$$

We then formulate the discretisation of (4) in the framework of Deconinck and Ricchiuto (2007) and apply the following steps.

1. In the computational domain Ω_h, replace the unknown U with an approximation U_h that is linear in every (triangular) cell and continuous over the entire domain.
2. Evaluate the discrete cell residual

$$\Phi_E = \int_E (\nabla \cdot \boldsymbol{F}(U_h) + S(U_h)) \, \mathrm{d}x \, \mathrm{d}y = \int_{\partial E} \boldsymbol{F}(U_h) \cdot \boldsymbol{n} \, \mathrm{d}s + \int_E S(U_h) \, \mathrm{d}x \, \mathrm{d}y, \tag{6}$$

   where $\boldsymbol{n}$ is the outward-pointing unit vector normal to the triangle.
3. Distribute the cell residual Φ_E (6) to the three vertices of the triangular cell in a conservative manner. That is, the fractions of the residual sent to vertex i are defined as

$$\Phi_i^E = \boldsymbol{\beta}_i^E \Phi_E, \tag{7}$$

   where $\boldsymbol{\beta}_i^E$ is a diagonal matrix so that $\sum_{i \in E} \boldsymbol{\beta}_i^E = \mathcal{I}$ with $\mathcal{I}$ being the identity matrix. Note that this means that every mesh-node residual receives contributions from its neighbouring cells only,

$$\Phi_i = \sum_{E \in D_i} \Phi_i^E, \qquad \forall i \in \Omega_h.$$

4. Impose boundary conditions by adding a flux difference to the boundary-node residual for the incoming characteristics, so that

$$\Phi_i = [\Phi_i]^+ + \sum_{E \in D_i} \Phi_i^E, \quad [\Phi_i] = (\boldsymbol{F}(U_b) - \boldsymbol{F}(U_i)) \cdot \boldsymbol{n}_i^b, \qquad \forall i \in \partial\Omega_h, \tag{8}$$

where U_b is the boundary condition and the superscript $^+$ denotes the fact that the flux difference is added only for the incoming characteristics. We discuss the imposition of boundary conditions in more detail in Section 3.3.

5. Solve the algebraic system

$$\Phi_i = 0, \qquad \forall i \in \Omega_h \tag{9}$$

at each time step.

Each of the above steps influences the properties of the numerical scheme. Depending on the specific physical application, a successful numerical discretisation using a linear representation should have the following properties: positivity, second-order accuracy, conservation, upwinding, well-balancedness and computational efficiency. For a more thorough discussion, see Hubbard (2008), Hubbard and Ricchiuto (2011) or Sármány et al. (2012).

3.1. Evaluation of the cell residual

By choosing the conservative variables U as the ones that vary linearly within each triangle, it is not possible to compute the flux integral $\int_E \nabla \cdot \boldsymbol{F}(U_h)$ in a conservative manner by using a single quadrature point. Instead, in order to achieve conservation, we apply Simpson's rule to the boundary integral

$$\int_{\partial E} \boldsymbol{F}(U_h) \cdot \boldsymbol{n} \, \mathrm{d}s = \sum_{l \in E} \frac{|l|}{6} \left(\boldsymbol{F}(U_1^l) + 4\boldsymbol{F}(\tfrac{1}{2}U_1^l + \tfrac{1}{2}U_2^l) + \boldsymbol{F}(U_2^l) \right) \cdot \boldsymbol{n}_l,$$

where $\boldsymbol{n}_l$ is the outward-pointing unit vector with length of the side l, while U_1^l and U_2^l are the values of U_h at the endpoints of the side l. Note that this evaluation is sufficiently accurate for linearly varying U_h.

The evaluation of the source-term integral $\int_E S(U_h)$ is often motivated by the preservation of the balance properties. In the current study we take

$$\int_E S(U_h) \, \mathrm{d}x \, \mathrm{d}y \approx$$
$$-\frac{1}{2} g \overline{d} \sum_{i \in E} \begin{bmatrix} 0 \\ b_i \boldsymbol{n}_i \end{bmatrix} + \overline{f} \frac{|E|}{3} \sum_{i \in E} \begin{bmatrix} 0 \\ d\boldsymbol{u}_i^\perp \end{bmatrix} - \frac{1}{\rho} \frac{|E|}{3} \sum_{i \in E} \begin{bmatrix} 0 \\ \boldsymbol{\tau}_i \end{bmatrix} + \gamma \frac{|E|}{3} \sum_{i \in E} \begin{bmatrix} 0 \\ d\boldsymbol{u}_i \end{bmatrix}, \tag{10}$$

where $\overline{\cdot}$ denotes the arithmetic mean over the cell, $\boldsymbol{n}_i$ is the outward-pointing normal vector opposite node i with length of the edge opposite node i, $|E|$ is the area of the triangle, and $\boldsymbol{u}^\perp = [-v, u]^T$. As the results in Sármány et al. (2012) show, the evaluation (10) ensures that the hydrostatic balance is exactly preserved for many of the RD schemes. However, (10) does not, in general, satisfy the geostrophic balance exactly. To be able to do that on triangular meshes, a mixed formulation of one form or another is required, see for example Cotter et al. (2009).

3.2. Distribution of the cell residual

Out of the large number of numerical schemes that can be recast in the RD framework, we now describe two linear schemes that satisfy the multidimensional upwinding and conservation properties. Being linear, Godunov (1959) proved that these schemes cannot be both positive and second-order accurate. When necessary, however, this property can be achieved by applying nonlinear blending on these two schemes. This can also be viewed as a form of limiting.

To describe these schemes, we first introduce the upwind parameter

$$\mathcal{K}_i = -\frac{1}{2}\overline{\boldsymbol{\mathcal{A}}} \cdot \boldsymbol{n}_i,$$

where $\overline{\boldsymbol{\mathcal{A}}} = \boldsymbol{\mathcal{A}}(\overline{U})$ and $\boldsymbol{n}_i$ is, as before, the outward-pointing normal vector opposite node i with length of the edge opposite node i. Assuming that $\mathcal{K}_i$ is diagonalisable, we have

$$\begin{aligned} \mathcal{K}_i &= \left(\mathcal{R}\mathcal{D}\mathcal{R}^{-1}\right)_i, \qquad & \mathcal{K}_i^- &= \left(\mathcal{R}\mathcal{D}^-\mathcal{R}^{-1}\right)_i, \\ \mathcal{K}_i^+ &= \left(\mathcal{R}\mathcal{D}^+\mathcal{R}^{-1}\right)_i, \qquad & \mathcal{N} &= \left(\sum_{i\in E}\mathcal{K}_i^+\right)^{-1}, \end{aligned} \tag{11}$$

where $\mathcal{D}$ is the diagonal matrix with the eigenvalues of $\mathcal{K}_i$, and $\mathcal{R}^{-1}$ and $\mathcal{R}$ are the matrices that contain the left and right eigenvectors, respectively. Furthermore, $\mathcal{D}^{\pm} = \frac{1}{2}\left(\mathcal{D} \pm |\mathcal{D}|\right)$, where $|\mathcal{D}|$ denotes the absolute values of the entries. Then the schemes used in this work are as follows.

- *The LDA* (low-diffusion A) scheme of Roe (1987) (see also Ricchiuto et al. (2005)) is defined as

$$\Phi_i^{LDA} = \mathcal{K}_i^+ \mathcal{N} \Phi_E. \tag{12}$$

  This is an upwind, conservative and second-order accurate scheme, which lacks positivity and is therefore unsuitable for capturing discontinuities in the solution.
- *The N* (narrow) scheme of Roe (1987) here is defined as in Sármány et al. (2012) so that the hydrostatic balance is satisfied exactly,

$$\Phi_{i,E}^N = \Phi_{i,E}^{LDA} + \mathcal{K}_i^+ \mathcal{N} \sum_{j\in E} \mathcal{K}_j^+ \left(V_i - V_j\right), \tag{13}$$

  where $V = [\eta, du, dv]^T$. This is a linear scheme that is conservative and exhibits oscillation-free behaviour, but it is also rather diffusive, making it less attractive for the resolution of linear or weakly nonlinear waves.
- *The B* (blended) scheme is defined so that it combines the N and LDA schemes through a nonlinear blending coefficient,

$$\Phi_{i,E}^B = \Theta \Phi_{i,E}^N + \left(\mathcal{I} - \Theta\right) \Phi_{i,E}^{LDA}, \tag{14}$$

  where $\mathcal{I}$ is the identity matrix and Θ is a diagonal matrix with the blending coefficients in the diagonal. The blending coefficients determine how 'well' the required properties, especially oscillation-free behaviour, are satisfied. The approach adopted in this article is from Abgrall and Mezine (2003) and it consists of: *a)* choosing a

particular direction $\boldsymbol{\xi} = (\xi_x, \xi_y)$; *b)* using the decomposition $\overline{\boldsymbol{\mathcal{A}}} \cdot \boldsymbol{\xi} = \mathcal{R}_\xi \mathcal{D}_\xi \mathcal{R}_\xi^{-1}$ to compute the 'characteristic' residuals

$$\Phi_i^{LDA} = \mathcal{R}_\xi^{-1} \Phi_i^{LDA}, \quad \Phi_i^N = \mathcal{R}_\xi^{-1} \Phi_i^N;$$

c) computing the blending coefficients as in Deconinck et al. (2000)

$$\Theta = \mathrm{diag}\left(\frac{\left| \sum_{i \in E} \Phi_i^N \right|}{\sum_{i \in E} |\Phi_i^N|} \right); \tag{15}$$

and, finally, *d)* applying (14) on the characteristic residuals. The blended residual on the original variables can then be calculated as $\Phi_i^B = \mathcal{R}_\xi \Phi_i^B$. Throughout this work, we make the typical choice of setting $\boldsymbol{\xi} = \frac{\boldsymbol{u}}{|\boldsymbol{u}|}$ for the cell distribution.

3.3. Boundary conditions

To impose the boundary condition (8), we first need to define the outward-pointing normal $\boldsymbol{n}_i^b$ for each boundary node. This is given as

$$\boldsymbol{n}_i^b = \frac{\left|\boldsymbol{n}_i^L\right| + \left|\boldsymbol{n}_i^R\right|}{|\boldsymbol{n}_i^L + \boldsymbol{n}_i^R|} \frac{\boldsymbol{n}_i^L + \boldsymbol{n}_i^R}{2},$$

where $\boldsymbol{n}_i^L$ and $\boldsymbol{n}_i^R$ are the outward-pointing normals of the two boundary edges that connect at $\boldsymbol{n}_i^b$. Note that this definition satisfies $\sum_{i \in \partial\Omega_h} \left|\boldsymbol{n}_i^b\right| = |\partial\Omega_h|$. To be able to determine the incoming part of the shallow-water spectrum, we use a similar eigenvalue decomposition as for the distribution of the cell residuals in the B scheme,

$$\overline{\boldsymbol{\mathcal{A}}}_b \cdot \boldsymbol{\xi} = \mathcal{R}_\xi \mathcal{D}_\xi \mathcal{R}_\xi^{-1}, \qquad \boldsymbol{\xi} = -\frac{\boldsymbol{n}_i^b}{\left|\boldsymbol{n}_i^b\right|},$$

where $\overline{\boldsymbol{\mathcal{A}}}_b = \boldsymbol{\mathcal{A}}\left(\frac{U_b + U_i}{2}\right)$. The flux difference to be added to each node residual at the boundary is then given as

$$\left[\Phi_i\right]^+ = \mathcal{R}_\xi \left(\mathrm{sgn}\, \mathcal{D}_\xi^+\right) \mathcal{R}_\xi^{-1} \left[\Phi_i\right], \qquad \forall i \in \partial\Omega_h,$$

where $\mathrm{sgn}\, \mathcal{D}_\xi^+$ denotes the sign function applied to the entries of $\mathcal{D}_\xi^+$.

The boundary values U_b are often imposed externally as predetermined values based on some assumptions, an exact solution or just provided by a previous forecast in actual simulations. Solid-wall boundary conditions $\boldsymbol{u} \cdot \boldsymbol{n} = 0$ are imposed by the mirror principle, so that $d_b = d_h$, $\boldsymbol{u}_b = \boldsymbol{u}_h - 2\left(\boldsymbol{u} \cdot \boldsymbol{n}\right) \boldsymbol{n}$. When the test case requires a sponge – or absorbing – boundary condition, which is neither transmissive nor reflective, we simply set the boundary condition to be that of supercritical outflow. This often acts as a very simple sponge boundary condition thanks to the numerical diffusion that is already in the discretisation.

4. Space-time discontinuous residual distribution

For the space-time discontinuous scheme we consider the full time-dependent system

$$\partial_t U + \nabla \cdot \boldsymbol{F}(U) + S(U) = 0 \qquad \text{or} \qquad \partial_t U + \boldsymbol{\mathcal{A}}(U) \cdot \nabla U + S(U) = 0 \tag{16}$$

with appropriate initial and boundary conditions. As in the steady case, $\boldsymbol{F}(U)$ represents the flux Jacobian and $\boldsymbol{\mathcal{A}}(U) = [\mathcal{A}_x, \mathcal{A}_y] = [\partial F_x/\partial U, \partial F_y/\partial U] = \partial \boldsymbol{F}/\partial U$ is the wave-speed tensor. The space-time prism residual is then given as

$$\Phi_{E_t} = \int_{t^n}^{t^{n+1}} \int_{E} \left(\partial_t U + \nabla \cdot \boldsymbol{F}(U) + S(U)\right) \mathrm{d}x \, \mathrm{d}y \, \mathrm{d}t \tag{17}$$

so that

$$\Phi_t = \int_{t^n}^{t^{n+1}} \int_{\Omega_h} \left(\partial_t U + \nabla \cdot \boldsymbol{F}(U) + S(U)\right) \mathrm{d}x \, \mathrm{d}y \, \mathrm{d}t = \sum_{E \in \Omega_h} \Phi_{E_t}$$

in every solution layer $[t^n, t^{n+1}] \times \Omega_h$. The discretisation steps are now similar to the steady case in Section 3.

1. In the computational domain Ω_h, replace the unknown U with an approximation U_h that is both linear in every (triangular) cell and linear in time. The discrete representation U_h is designed to be continuous in space but allowed to be discontinuous in time.
2. Evaluate the discrete prism residual, using the trapezium rule in time, as

$$\begin{aligned}
\Phi_{E_t} &= \int_{t^n}^{t^{n+1}} \int_{E} \left(\partial_t U + \nabla \cdot \boldsymbol{F}(U) + S(U)\right) \mathrm{d}x \, \mathrm{d}y \, \mathrm{d}t \\
&\approx \int_{E} \left(U_h^{n+1} - U_h^n\right) \mathrm{d}x \, \mathrm{d}y + \frac{\Delta t}{2} \left(\int_{\partial E} \boldsymbol{F}(U^n) \cdot \boldsymbol{n} \, \mathrm{d}s + \int_{\partial E} \boldsymbol{F}(U^{n+1}) \cdot \boldsymbol{n} \, \mathrm{d}s \right) \\
&= \int_{E} \left(U_h^{n+1} - U_h^n\right) \mathrm{d}x \, \mathrm{d}y + \frac{\Delta t}{2} (\Phi_E^n + \Phi_E^{n+1}),
\end{aligned} \tag{18}$$

   where $\boldsymbol{n}$ is the outward-pointing unit vector normal to the edge. The residuals Φ_E^n and Φ_E^{n+1} are calculated precisely as in the steady case described in Section 3.1.
3. Distribute the prism residual Φ_{E_t} (18) to the six vertices of the prism in a conservative manner. That is, the fractions of the residual sent to vertex i at time levels n and $n+1$ are defined as

$$\Phi_{i,n}^E = \boldsymbol{\beta}_{i,n}^E \Phi_{E_t} \quad \text{and} \quad \Phi_{i,n+1}^E = \boldsymbol{\beta}_{i,n+1}^E \Phi_{E_t}, \tag{19}$$

   where $\boldsymbol{\beta}_{i,n}^E$ and $\boldsymbol{\beta}_{i,n+1}^E$ are diagonal matrices and $\sum_{i \in E} \boldsymbol{\beta}_{i,n}^E + \sum_{i \in E} \boldsymbol{\beta}_{i,n+1}^E = \mathcal{I}$.

4. At time level t^n, add the contribution from the time discontinuity (see Hubbard and Ricchiuto (2011) and Sármány et al. (2012)) as

$$\Psi^E_{i,n} = \frac{|E|}{3}\left[U^n_i\right], \tag{20}$$

where $[\cdot]$ denotes the jump across the time discontinuity. For the first time step, the initial condition is used as the value from the 'previous time step', i.e. $[U^0_i] = U^0_i - U_i(0)$, where U^0_i is the numerical value and $U_i(0)$ is the initial condition.

5. Impose the boundary condition by adding a flux difference to each boundary node at both time levels t^n and t^{n+1}, so that

$$\begin{aligned} \Phi^n_i &= \frac{\Delta t}{2}\left[\Phi^n_i\right]^+ + \sum_{E\in D_i}\left(\Phi^E_{i,n} + \Psi^E_{i,n}\right), \qquad \forall i \in \partial\Omega_h, \\ \Phi^{n+1}_i &= \frac{\Delta t}{2}\left[\Phi^{n+1}_i\right]^+ + \sum_{E\in D_i}\Phi^E_{i,n+1}, \qquad \forall i \in \partial\Omega_h, \end{aligned} \tag{21}$$

where the flux differences through the boundary are calculated exactly as in the steady-state case, cf. (8).

6. Solve the algebraic system

$$\Phi^n_i = 0, \quad \Phi^{n+1}_i = 0, \qquad \forall i \in \Omega_h \tag{22}$$

at each time step.

Remark. As a consequence of the discontinuous representation in time, there is no stability restriction on the time step Δt in the current formulation. This contrasts with the fully continuous scheme, where the condition

$$\max \operatorname{diag} \mathcal{D}_{i,n} \leq 0, \qquad \forall i \in E \subset \Omega_h$$

needs to be satisfied as shown in Deconinck and Ricchiuto (2007). In the discontinuous case, the choice of Δt is driven solely by considerations about accuracy and performance of the algebraic solver. An extensive study into the role of the size of Δt is carried out for the non-rotating shallow-water system in Sármány et al. (2012). Our choice of the time step – which is twice as large as the maximum that the above formula would allow for the continuous case – is based on those results.

4.1. Distribution of the prism residual

For space-time prisms, the inflow parameters used for the prism distribution are defined as

$$\begin{aligned} \mathcal{K}_{i,n} &= -\frac{\Delta t}{4}\overline{\boldsymbol{\mathcal{A}}}\cdot\boldsymbol{n}_i - \frac{|E|}{3}\mathcal{I}, \\ \mathcal{K}_{i,n+1} &= -\frac{\Delta t}{4}\overline{\boldsymbol{\mathcal{A}}}\cdot\boldsymbol{n}_i + \frac{|E|}{3}\mathcal{I}, \end{aligned} \tag{23}$$

where $\mathcal{I}$ is the identity matrix and $\overline{\boldsymbol{\mathcal{A}}}$ represents a prism-averaged state of the flux Jacobian $\boldsymbol{\mathcal{A}}$. Assuming that the inflow matrices in (23) are diagonalisable just as they are in the

steady case, we can introduce the remaining inflow space-time parameters (cf. (11)),

$$\begin{aligned}
\mathcal{K}^+_{i,n} &= \left(\mathcal{R}\mathcal{D}^+\mathcal{R}^{-1}\right)_{i,n}, \quad \mathcal{K}^+_{i,n+1} = \left(\mathcal{R}\mathcal{D}^+\mathcal{R}^{-1}\right)_{i,n+1}, \\
\mathcal{K}^-_{i,n} &= \left(\mathcal{R}\mathcal{D}^-\mathcal{R}^{-1}\right)_{i,n}, \quad \mathcal{K}^-_{i,n+1} = \left(\mathcal{R}\mathcal{D}^-\mathcal{R}^{-1}\right)_{i,n+1}, \\
\mathcal{N}_t &= \left(\sum_{i\in E}\mathcal{K}^+_{i,n} + \sum_{i\in E}\mathcal{K}^+_{i,n+1}\right)^{-1}.
\end{aligned} \tag{24}$$

These are used to define the upwind space-time RD schemes similarly to the steady case.

- *The space-time LDA* (STLDA) scheme is defined as

$$\left(\Phi^E_{i,n}\right)^{LDA} = \mathcal{K}^+_{i,n}\mathcal{N}_t\Phi_{E_t}, \qquad \left(\Phi^E_{i,n+1}\right)^{LDA} = \mathcal{K}^+_{i,n+1}\mathcal{N}_t\Phi_{E_t}. \tag{25}$$

- *The space-time N* (STN) scheme is again defined as in Sármány et al. (2012) so that it preserves the hydrostatic balance exactly,

$$\begin{aligned}
\left(\Phi^E_{i,n}\right)^{N} &= \left(\Phi^E_{i,n}\right)^{LDA} \\
&\quad + \mathcal{K}^+_{i,n}\mathcal{N}_t\sum_{j\in E}\mathcal{K}^+_{j,n}\left(V^n_i - V^n_j\right) + \mathcal{K}^+_{i,n}\mathcal{N}_t\sum_{j\in E}\mathcal{K}^+_{j,n+1}\left(V^{n+1}_i - V^{n+1}_j\right), \\
\left(\Phi^E_{i,n+1}\right)^{N} &= \left(\Phi^E_{i,n+1}\right)^{LDA} \\
&\quad + \mathcal{K}^+_{i,n+1}\mathcal{N}_t\sum_{j\in E}\mathcal{K}^+_{j,n}\left(V^n_i - V^n_j\right) + \mathcal{K}^+_{i,n+1}\mathcal{N}_t\sum_{j\in E}\mathcal{K}^+_{j,n+1}\left(V^{n+1}_i - V^{n+1}_j\right).
\end{aligned} \tag{26}$$

- *The space-time blended* (STB) scheme is now defined as a nonlinear interpolation between the STLDA and the STN schemes,

$$\begin{aligned}
\left(\Phi^E_{i,n}\right)^{B} &= \Theta\left(\Phi^E_{i,n}\right)^{N} + (\mathcal{I}-\Theta)\left(\Phi^E_{i,n}\right)^{LDA}, \\
\left(\Phi^E_{i,n+1}\right)^{B} &= \Theta\left(\Phi^E_{i,n+1}\right)^{N} + (\mathcal{I}-\Theta)\left(\Phi^E_{i,n+1}\right)^{LDA}.
\end{aligned} \tag{27}$$

  The blending is now carried out on the characteristic space-time residuals

$$\Phi^N_{i,n} = \mathcal{R}_\xi^{-1}\Phi^N_{i,n}, \quad \Phi^N_{i,n+1} = \mathcal{R}_\xi^{-1}\Phi^N_{i,n+1}, \quad \Phi^{LDA}_{i,n} = \mathcal{R}_\xi^{-1}\Phi^{LDA}_{i,n}, \quad \Phi^{LDA}_{i,n+1} = \mathcal{R}_\xi^{-1}\Phi^{LDA}_{i,n+1},$$

  with the blending parameter computed as

$$\Theta = \mathrm{diag}\left(\frac{\left|\sum_{i\in E}\Phi^N_{i,n} + \sum_{i\in E}\Phi^N_{i,n+1}\right|}{\sum_{i\in E}\left|\Phi^N_{i,n}\right| + \sum_{i\in E}\left|\Phi^N_{i,n+1}\right|}\right), \tag{28}$$

  where we have dropped the superscript 'E' to avoid clutter. Finally, we calculate the blended residuals based on the original variables by $\Phi^B_{i,n} = \mathcal{R}_\xi\Phi^B_{i,n}$ and $\Phi^B_{i,n+1} = \mathcal{R}_\xi\Phi^B_{i,n+1}$.

4.2. Boundary conditions

The imposition of the boundary conditions for the space-time scheme is precisely as described in Section 3.3, i.e. the pointwise flux differences $[\Phi^n_i]^+$ and $\left[\Phi^{n+1}_i\right]^+$ in (21) are computed by using the decomposition

$$\overline{\boldsymbol{\mathcal{A}}}_b\cdot\boldsymbol{\xi} = \mathcal{R}_\xi\mathcal{D}_\xi\mathcal{R}_\xi^{-1}, \qquad \boldsymbol{\xi} = -\frac{\boldsymbol{n}^b_i}{\left|\boldsymbol{n}^b_i\right|},$$

where $\overline{\boldsymbol{\mathcal{A}}}_b = \boldsymbol{\mathcal{A}}\left(\frac{U^n_b+U^n_i}{2}\right)$ for $[\Phi^n_i]^+$ and $\overline{\boldsymbol{\mathcal{A}}}_b = \boldsymbol{\mathcal{A}}\left(\frac{U^{n+1}_b+U^{n+1}_i}{2}\right)$ for $\left[\Phi^{n+1}_i\right]^+$.

5. Implementation details

For both steady-state and space-time computations, a nonlinear algebraic system of equations has to be solved. In the steady case, the system (9) needs to be solved only once, while for space-time simulations, the solution of the system (22) is required at each time step.

A simple explicit pseudo-time-stepping algorithm is used in both cases. For the steady-state scheme, this is given as

$$U_i^{m+1} = U_i^m - \frac{\tau}{s_i}\Phi_i^m, \qquad \forall i \in \Omega_h, \tag{29}$$

where s_i is the volume of the spatial dual cell and τ is the pseudo-time step. It is computed as

$$\tau = 0.9 \min_i \frac{s_i}{\sum_{E\in D_i} \varrho(\mathcal{K}_i^+)}, \qquad \varrho(\mathcal{K}_i^+) = \max \operatorname{diag} \mathcal{D}_i^+, \tag{30}$$

with $\varrho(\mathcal{M})$ denoting the spectral radius of a given matrix $\mathcal{M}$. Similarly, for the space-time computations the pseudo-time stepping takes the form

$$\begin{pmatrix} U_i^n \\ U_i^{n+1} \end{pmatrix}^{m+1} = \begin{pmatrix} U_i^n \\ U_i^{n+1} \end{pmatrix}^{m} - \frac{\tau}{s_i^t} \begin{pmatrix} \Phi_i^n \\ \Phi_i^{n+1} \end{pmatrix}^{m}, \qquad \forall i \in \Omega_h, \tag{31}$$

where $s_i^t = \Delta t s_i$ is the volume of the dual space-time prism. The pseudo-time step τ is now calculated as

$$\tau = 0.9 \min_i \frac{s_i^t}{\sum_{E\in D_i} \varrho(\mathcal{K}_{i,n+1}^+)}, \qquad \varrho(\mathcal{K}_{i,n+1}^+) = \max \operatorname{diag} \mathcal{D}_{i,n+1}^+, \tag{32}$$

where, as before, $\mathcal{K}_{i,n+1}^+$ and $\mathcal{D}_{i,n+1}^+$ are associated with the prism-averaged state as opposed to the cell-averaged one in (30).

Similarly to other iterative methods, it is often possible to solve the above algebraic systems up to machine precision. Nevertheless, a much less accurate solution is sufficient as long as the properties of the numerical scheme are not compromised. Consequently, for the steady-state problem in Section 6.4, we use the stopping criterion

$$\texttt{rel\_tol} = \frac{\|\Psi^m\|_1}{\|\Psi^0\|_1} < 10^{-8} \qquad \text{with} \qquad \Psi^m = \left\{ \frac{\tau}{s_i}\Phi_i^m \right\}_{i\in\Omega_h}, \qquad \forall m.$$

In space-time calculations, such accuracy is not necessary because of a good initial guess from the previous time step. For these test problems, we set the stopping criterion to

$$\texttt{rel\_tol} = \frac{\| \left(\Psi^n, \Psi^{n+1}\right)_m^T \|_1}{\| \left(\Psi^n, \Psi^{n+1}\right)_0^T \|_1} < 10^{-3}$$

with

$$\begin{pmatrix} \Psi^n \\ \Psi^{n+1} \end{pmatrix}^{m} = \left\{ \frac{\tau}{s_i^t} \begin{pmatrix} \Phi_i^n \\ \Phi_i^{n+1} \end{pmatrix}^{m} \right\}_{i\in\Omega_h}, \qquad \forall m.$$

5.1. Efficiency considerations

The above-described pseudo-time-stepping algorithms are solely a means of solving the systems of nonlinear algebraic equations (9) and (22), so they do not need to be accurate in (pseudo-)time. The size of the pseudo-time step τ is determined by the stability condition of the explicit Euler scheme and therefore the pseudo-CFL has to be smaller than one (hence our choice of 0.9). It would be possible to use other iterative methods – such as the Newton method – to solve the nonlinear algebraic systems. However, we prefer pseudo-time stepping for inviscid flows mainly because it is local, it avoids the need for assembling and solving a global system, and it is not sensitive to the initial guess. Its locality, in particular, means that the implementation on parallel architectures is relatively straightforward and it scales well. Each unknown is only connected to its nearest neighbours in space-time and that connectivity does not depend on the size of the time step Δt.

Its main drawback, however, is that the number of pseudo-time iterations required to reach the stopping criterion of 10^{-3} is large. For all time-dependent numerical tests considered here, that number falls in the region of 20 to 40. Although it is sometimes possible to take a larger stopping criterion, the value 10^{-3} is typically necessary for having negligible effect on the accuracy of the time-dependent approximation. This requirement is generally independent of the actual test case.

6. Numerical results

In this section, we present a range of test cases to validate the performance of the RD scheme applied to the rotating shallow-water equations. We solve the nonlinear system (1) for all the numerical simulations, but the exact solutions – when available – are derived through analytical approximations.

6.1. Equatorial Kelvin wave

This problem describes a wave travelling eastwards in equatorial regions. If the shallow-water system is linearised around a constant state of the primitive variables, an analytical solution can be obtained. We use an analytical solution of the nondimensional equations, taken from Eskilsson and Sherwin (2004) and Giraldo and Warburton (2008). It is given as

$$\begin{aligned} d(x,y,t) &= 1 + A\exp\left(-\frac{1}{2}y^2\right)\exp\left(-\frac{1}{2}\left(x+5-t\right)^2\right), \\ u(x,y,t) &= A\exp\left(-\frac{1}{2}y^2\right)\exp\left(-\frac{1}{2}\left(x+5-t\right)^2\right), \\ v(x,y,t) &= 0, \end{aligned} \tag{33}$$

where A is the amplitude of the wave, $f_0 = 0$, $\beta = 1$, $g = 1$, $b(x,y) \equiv 0$, $\gamma = 0$, $\boldsymbol{\tau} \equiv \mathbf{0}$ and $\Omega = [-10, 10] \times [-5, 5]$. Since we discretise the nonlinear equations, this analytical solution can only be used to assess the convergence of the numerical scheme as long as the error associated with the numerical discretisation is much larger than the error associated with the linearisation to obtain (33). This is typically the case if the amplitude is small. So in order to check grid convergence for the numerical scheme we set $A = 10^{-4}$ and

$A = 10^{-3}$, and integrate until $T = 10$ with initial condition given by (33) with $t = 0$. We use a sequence of four meshes with characteristic edge lengths of 1, $\frac{1}{2}$, $\frac{1}{4}$ and $\frac{1}{8}$. Figure 1 shows grid-convergence rates for the STLDA and the STB schemes. The left plot confirms second-order convergence for the STLDA scheme and slightly suboptimal convergence for the STB scheme, which tallies with existing results for both schemes when the solution is smooth, see Hubbard and Ricchiuto (2011) and Sármány et al. (2012). By comparison, the right plot shows that with $A = 10^{-3}$ the convergence rate, while maintained on coarser meshes, drops for the finest mesh when the STLDA scheme is used. This is because at this level the numerical error becomes comparable to that associated with the linearisation. The STB formulation does not exhibit this for any of the meshes used since it is less accurate overall.

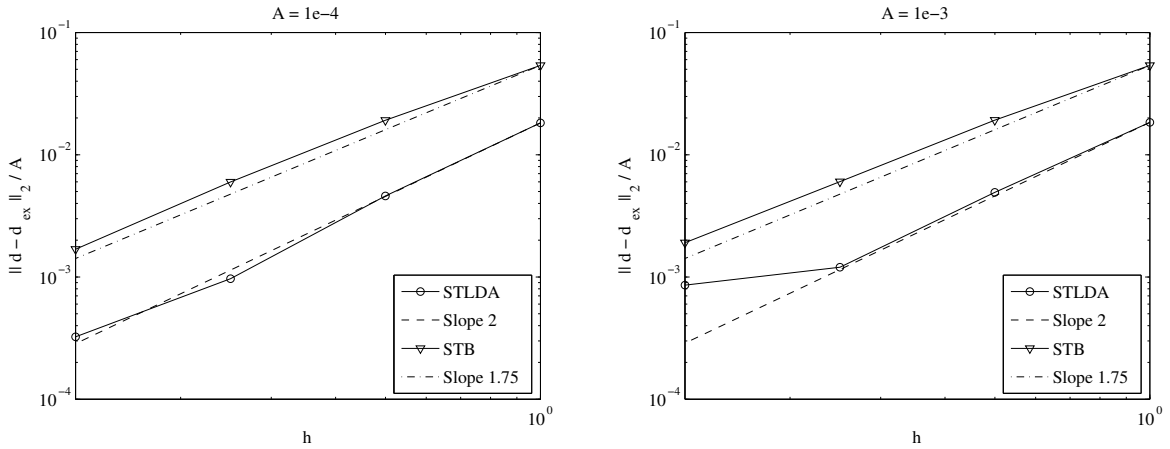

Figure 1: Equatorial Kelvin wave. Grid-convergence study of the error between the linear analytical and the nonlinear numerical solution for amplitudes 10^{-4} and 10^{-3}.

Based on these convergence results, we can infer that the STLDA and the STB schemes on the finest mesh approximate the equations with the respective accuracies of $\|d_h - d_{ex}\|_2/A \approx 10^{-3.5}$ and $\|d_h - d_{ex}\|_2/A \approx 10^{-2.8}$ independently of the amplitude. In Figure 2, we plot the nonlinear numerical results for $A = 10^{-4}$, $A = 10^{-3}$, $A = 10^{-2}$, $A = 10^{-1}$ and compare them to the linear analytical results. They show that the 'visible' effects of nonlinearity begin to appear for $A = 10^{-2}$ and become obvious for $A = 10^{-1}$. The results of the STLDA and STB schemes look qualitatively identical so we only present the results obtained with the STLDA method.

6.2. Equatorial nonlinear Rossby soliton

This example is an equatorial trapped nonlinear wave travelling westwards. The exact solution is not known but an analytical approximation can be derived through the method of multiple scales as shown in Boyd (1985). For the primitive variables, this is given as

$$
\begin{aligned}
d(x, y, t) &= d^{(0)} + d^{(1)} \\
u(x, y, t) &= u^{(0)} + u^{(1)} \\
v(x, y, t) &= v^{(0)} + v^{(1)},
\end{aligned}
$$

where the superscripts (0) and (1) denote the zeroth-order and the first-order wave mode in the analytical solution, respectively. These are given as

$$
\begin{aligned}
d^{(0)} &= 1 + \frac{1}{4}(6y^2 + 3)\kappa \mathrm{e}^{-\frac{y^2}{2}} \\
u^{(0)} &= \frac{1}{4}(6y^2 - 9)\kappa \mathrm{e}^{-\frac{y^2}{2}} \\
v^{(0)} &= 2y\frac{\partial \kappa}{\partial \zeta}\mathrm{e}^{-\frac{y^2}{2}}
\end{aligned}
$$

and

$$
\begin{aligned}
d^{(1)} &= \frac{9}{16}C_1(2y^2 - 5)\kappa \mathrm{e}^{-\frac{y^2}{2}} + \kappa^2 \tilde{d}(y) \\
u^{(1)} &= \frac{9}{16}C_1(2y^2 + 3)\kappa \mathrm{e}^{-\frac{y^2}{2}} + \kappa^2 \tilde{u}(y) \\
v^{(1)} &= \kappa\frac{\partial \kappa}{\partial \zeta}\tilde{v}(y),
\end{aligned}
$$

where $\kappa(\zeta) = A\cosh^{-2}(B\zeta)$, $\zeta = x - Ct$, $B = 0.394$, $A = 0.771B^2$, $C = C_0 + C_1$, $C_0 = -\frac{1}{3}$ and $C_1 = -0.395B^2$. The variable κ is the solution to the Korteweg–de Vries (KdV) equation, which describes the behaviour of solitons. As shown in Boyd (1980), under certain conditions the shallow-water equations reduce to the KdV equation by using the method of multiple scales. The tilde terms above are computed as

$$
\begin{bmatrix} \tilde{d}(y) \\ \tilde{u}(y) \\ \tilde{v}(y) \end{bmatrix} = \mathrm{e}^{-\frac{y^2}{2}} \sum_{n=0}^{\infty} \begin{bmatrix} \hat{d}(y) \\ \hat{u}(y) \\ \hat{v}(y) \end{bmatrix} H_n(y) \approx \mathrm{e}^{-\frac{y^2}{2}} \sum_{n=0}^{26} \begin{bmatrix} \hat{d}(y) \\ \hat{u}(y) \\ \hat{v}(y) \end{bmatrix} H_n(y),
$$

where $H_n(y)$ are the Hermite polynomials and $\hat{d}(y)$, $\hat{u}(y)$, $\hat{v}(y)$ are the unnormalised Hermite coefficients given originally in Boyd (1985) but also to be found in Eskilsson and Sherwin (2004). The truncation of the series at $n = 26$ is exact in a computational sense because the resulting error is well below machine precision.

The numerical simulations are carried out in the domain $\Omega = [-24, 24] \times [-8, 8]$ until final time $T = 40$. Solid-wall conditions are used at the top and bottom parts of the boundary while characteristic inflow/outflow conditions are imposed at the left and right parts of the boundary. As in the case of the Kelvin wave, the parameters are set as $f_0 = 0$, $\beta = 1$, $g = 1$, $b(x, y) \equiv 0$, $\gamma = 0$ and $\boldsymbol{\tau} \equiv \mathbf{0}$.

Since the analytical solution is only a first-mode approximation, it cannot be used to assess grid convergence – not even in the way we do it for the equatorial Kelvin wave. Nevertheless, it is worth comparing the numerical phase speed with that of the analytical solution as well as checking whether the numerical solution captures the main features of the soliton.

Figures 3 and 4 show numerical solutions computed with the STLDA and STB schemes on a mesh with 113830 triangles. The analytical solution yields a peak of 1.162 at $(x, y) = (-15.77, 1.23)$. Both the STLDA and the STB schemes capture the phase speed quite accurately. The general shape of the wave is also preserved, although both schemes emit low-amplitude gravity waves. This is a feature that is in part the result of a non-exact initial condition and in part associated with many higher-order numerical schemes, see

Eskilsson and Sherwin (2004) and Giraldo and Warburton (2008). Overall, we observe little qualitative difference between the solutions obtained by the two schemes.

6.3. Nonlinear adjustment of a front

This example describes the evolution of a pressure discontinuity over an escarpment, similar to the one in Bouchut et al. (2008). The computational domain is $\Omega = [-30, 10]^2$, the bottom topography is defined as

$$b(x,y) = \begin{cases} 0.5 & \text{if} \quad y \leq -2.5, \\ 0.1(2.5 - y) & \text{if} \quad -2.5 < y < 2.5, \\ 0 & \text{if} \quad y \geq 2.5, \end{cases}$$

and the initial condition is given by

$$\boldsymbol{u}_0 = \mathbf{0}, \qquad d_0(x,y) = \begin{cases} 1.1 & \text{if} \quad x < 0, \\ 1 & \text{if} \quad \text{otherwise.} \end{cases}$$

This problem is also solved as the nondimensionalised system but using the f_0-plane approximation rather than the β-plane one. The parameters are thus defined as $f_0 = 1$, $\beta = 0$, $g = 1$, $\gamma = 0$ and $\boldsymbol{\tau} = \mathbf{0}$. Still-water boundary conditions are imposed by means of characteristics at the left and right boundaries, while absorbing boundary conditions are used for the top and bottom boundaries to indicate middle-of-the-ocean situations.

Since the initial condition contains a discontinuity, we use the STB scheme to eliminate unphysical oscillations around the discontinuity. Figures 5 and 6 show contour and slice plots, respectively, at six different times. The results show that the expected behaviour after the initial discontinuity is captured, see Bouchut et al. (2008). First, fast inertia-gravity waves are emitted from the area of the discontinuity and they leave the domain at different speeds because of the varying bottom topography. Second, a jet forms along the initial discontinuity. Third, a trapped topographic Rossby wave develops around the intersection of the initial discontinuity and the escarpment. Since $f > 0$ (northern hemisphere), it travels such that the shallower water is on the right. Last, a packet of short waves is also created that travels in the opposite direction to the wave tongue.

6.4. Nonlinear Stommel problem

This is the only steady-state problem that we consider in this work. It describes a situation when the wind stress, bottom friction, Coriolis force and the nonlinear advective term are in balance. In this case, we solve the dimensional system (1) in the domain $\Omega = [0, 10^6]^2$ with parameters $f_0 = 10^{-4}$, $\beta = 10^{-11}$, $g = 9.80665$, $\gamma = 10^{-6}$, $\boldsymbol{\tau} = 0.2\,[\cos(\pi y), 0]^T$, $b(x,y) \equiv 0$. The initial condition is that of a still lake $[\eta, du, dv]^T = [d, du, dv]^T = [1000, 0, 0]^T$, while the boundary conditions are solid wall everywhere.

Since the solution of this problem is smooth and the nonlinearity is weak, we only consider the STLDA scheme. The results in Figure 7 show an accumulation of water at the northwesterly part of the domain – in line with observations of oceanic currents and with recent numerical results obtained by the DG method, see for example Giraldo and Warburton (2008), Comblen et al. (2010) and Escobar-Vargas et al. (2012).

7. Concluding remarks and outlook

This article has introduced the framework of residual distribution (RD) to shallow-water ocean modelling. While the method has a relatively long history in computational fluid dynamics, this is – to our knowledge – the first time it has been successfully applied to the rotating shallow-water equations. It shares many similarities with other numerical methods suitable for unstructured triangular meshes, such as finite volumes or finite elements. It has, however, significant advantages over those methods in situations when both nonlinear dynamics and the preservation of certain balance properties are important. The formulation presented here preserves only the hydrostatic balance exactly (over any shape of topography) but not the geostrophic balance because all unknown fields are stored at the vertices of the triangles. However, the upwinding character of the scheme, together with the fact that there are the same number of (vector-valued) unknowns for the velocity field as (scalar-valued) unknowns for the water height, suggests that the scheme is expected to be free of both spurious pressure and inertial modes. We have, indeed, detected no such spurious modes in the space-time simulations, but a Fourier analysis into the spectral properties of the linearised shallow-water equations remains to be conducted.

The main drawback of the proposed space-time RD formulation is that it is computationally relatively expensive. Although it is shown in Sármány et al. (2012) to outperform other implicit RD schemes, it is generally still more computationally intensive than most explicit approaches. Future research efforts will concentrate on including a moving-mesh algorithm that both reduces the number of pseudo-time iterations in the algebraic solver and the number of total degrees of freedom required to achieve the same quality of the solution.

References

Abgrall, R., 2012. A review of residual distribution schemes for hyperbolic and parabolic problems: the July 2010 state of the art. Commun. Comput. Phys. 11, 1043–1080.

Abgrall, R., Mezine, M., 2003. Construction of second order accurate monotone and stable residual distribution schemes for unsteady flow problems. J. Comput. Phys. 188, 16–55.

Audusse, E., Bouchut, F., Bristeau, M.O., Klein, R., Perthame, B., 2004. A fast and stable well-balanced scheme with hydrostatic reconstruction for shallow water flows. SIAM J. Sci. Comput. 25, 2050–2065.

Bouchut, F., 2007. Chapter 4 Efficient numerical finite volume schemes for shallow water models, in: Zeitlin, V. (Ed.), Nonlinear Dynamics of Rotating Shallow Water: Methods and Advances. Elsevier Science. volume 2 of *Edited Series on Advances in Nonlinear Science and Complexity*, pp. 189–256.

Bouchut, F., Scherer, E., Zeitlin, V., 2008. Nonlinear adjustment of a front over escarpment. Physics of Fluids 20.

Boyd, J.P., 1980. Equatorial solitary waves. Part 1: Rossby solitons. Journal of Physical Oceanography 10, 1699–1717.

Boyd, J.P., 1985. Equatorial solitary waves. Part 3: Westward-traveling modons. Journal of Physical Oceanography 15, 46–54.

Comblen, R., Lambrechts, J., Remacle, J.F., Legat, V., 2010. Practical evaluation of five partly discontinuous finite element pairs for the non-conservative shallow water equations. Internat. J. Numer. Methods Fluids 63, 701–724.

Cotter, C.J., Ham, D.A., Pain, C.C., 2009. A mixed discontinuous/continuous finite element pair for shallow-water ocean modelling. Ocean Modelling 26, 86–90.

Csík, Á., Deconinck, H., 2002. Space-time residual distribution schemes for hyperbolic conservation laws on unstructured linear finite elements. Internat. J. Numer. Methods Fluids 40, 573–581. ICFD Conference on Numerical Methods for Fluid Dynamics, Part II (Oxford, 2001).

Deconinck, H., Ricchiuto, M., 2007. Residual distribution schemes: foundation and analysis, in: Encyclopedia of computational mechanics. Wiley. volume 3.

Deconinck, H., Roe, P.L., Struijs, R., 1993. A multidimensional generalization of Roe's flux difference splitter for the Euler equations. Comput. & Fluids 22, 215–222.

Deconinck, H., Sermeus, K., Abgrall, R., 2000. Status of multidimensional upwind residual distribution schemes and applications in aeronautics, in: AIAA Paper 2000-2328, AIAA.

Escobar-Vargas, J.A., Diamessis, P.J., Giraldo, F.X., 2012. High-order discontinuous element-based schemes for the inviscid shallow water equations: spectral multidomain penalty and discontinuous Galerkin methods. Appl. Math. Comput. 218, 4825–4848.

Eskilsson, C., Sherwin, S.J., 2004. A triangular spectral/*hp* discontinuous Galerkin method for modelling 2D shallow water equations. Internat. J. Numer. Methods Fluids 45, 605–623.

Ford, R., Pain, C., Piggott, M., Goddard, A., de Oliveira, C., Umpleby, A., 2004a. A nonhydrostatic finite-element model for three-dimensional stratified oceanic flows. Part I: Model formulation. Monthly Weather Review 132, 2816–2831.

Ford, R., Pain, C., Piggott, M., Goddard, A., de Oliveira, C., Umpleby, A., 2004b. A nonhydrostatic finite-element model for three-dimensional stratified oceanic flows. Part II: Model validation. Monthly Weather Review 132, 2832–2844.

Fringer, O., Gerritsen, M., Street, R., 2006. An unstructured-grid, finite-volume, nonhydrostatic, parallel coastal ocean simulator. Ocean Modelling 14, 139–173.

Giraldo, F.X., Taylor, M.A., 2006. A diagonal-mass-matrix triangular-spectral-element method based on cubature points. J. Engrg. Math. 56, 307–322.

Giraldo, F.X., Warburton, T., 2008. A high-order triangular discontinuous Galerkin oceanic shallow water model. Internat. J. Numer. Methods Fluids 56, 899–925.

Godunov, S.K., 1959. A difference method for numerical calculation of discontinuous solutions of the equations of hydrodynamics. Mat. Sb. (N.S.) 47 (89), 271–306.

Hubbard, M.E., 2008. Discontinuous fluctuation distribution. J. Comput. Phys. 227, 10125–10147.

Hubbard, M.E., Ricchiuto, M., 2011. Discontinuous upwind residual distribution: A route to unconditional positivity and high order accuracy. Computers & Fluids 46, 263–269. 10th Institute for Computational Fluid Dynamics (ICFD) Conference, Univ Reading, England, 2010.

Iskandarani, M., Haidvogel, D.B., Levin, J.C., 2003. A three-dimensional spectral element model for the solution of the hydrostatic primitive equations. J. Comput. Phys. 186, 397–425.

Ma, H., 1993. A spectral element basin model for the shallow water equations. J. Comput. Phys. 109, 133–149.

Maddison, J., Marshall, D., Pain, C., Piggott, M., 2011. Accurate representation of geostrophic and hydrostatic balance in unstructured mesh finite element ocean modelling. Ocean Modelling 39, 248–261.

Ricchiuto, M., 2011a. Explicit residual discretizations for shallow water flows, in: Proceedings of ICNAAM 2011, 9th International Conference on Numerical Analysis and Applied Mathematics, Halkidiki (Greece).

Ricchiuto, M., 2011b. On the C-property and generalized C-property of residual distribution for the shallow water equations. J. Sci. Comput. 48, 304–318.

Ricchiuto, M., Abgrall, R., Deconinck, H., 2007. Application of conservative residual distribution schemes to the solution of the shallow water equations on unstructured meshes. J. Comput. Phys. 222, 287–331.

Ricchiuto, M., Bollermann, A., 2009. Stabilized residual distribution for shallow water simulations. J. Comput. Phys. 228, 1071–1115.

Ricchiuto, M., Csík, Á., Deconinck, H., 2005. Residual distribution for general time-dependent conservation laws. J. Comput. Phys. 209, 249–289.

Roe, P.L., 1982. Fluctuations and signals, in: K.W. Morton, M.J. Baines (Eds.), Numerical Methods for Fluid Dynamics. Academic Press, pp. 219–257.

Roe, P.L., 1987. Linear advection schemes on triangular meshes. Technical Report CoA 8720. Cranfield Institute of Technology.

Sármány, D., Hubbard, M., Ricchiuto, M., 2012. Unconditionally stable space-time discontinuous residual distribution for shallow-water flows. Technical Report RR-7958. INRIA. Submitted to Journal of Computational Physics.

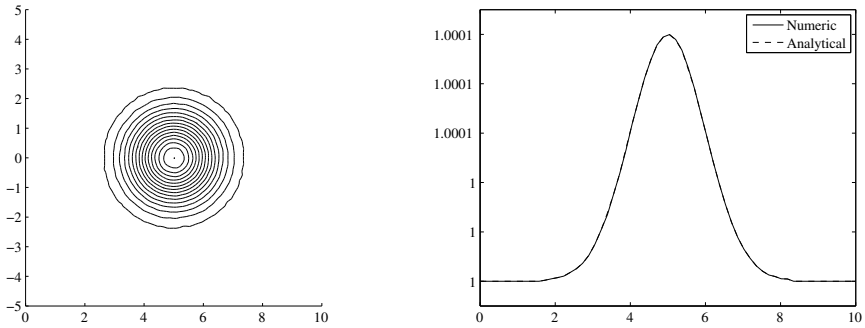

(a) $A = 10^{-4}$

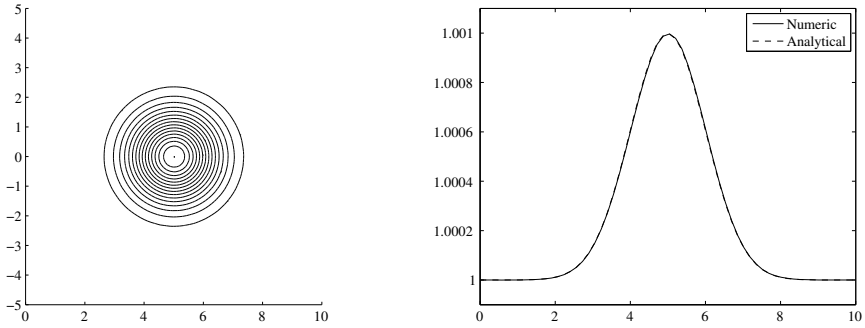

(b) $A = 10^{-3}$

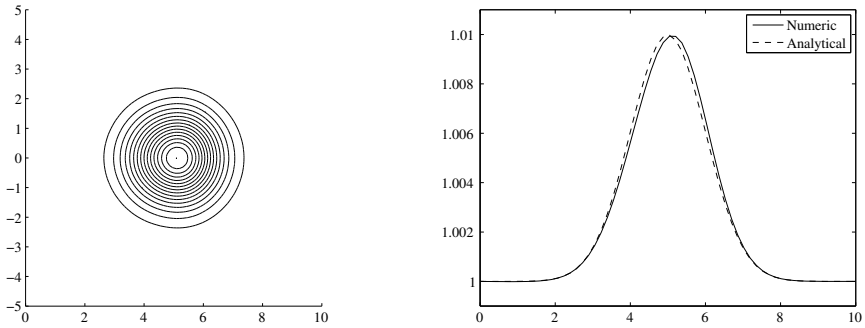

(c) $A = 10^{-2}$

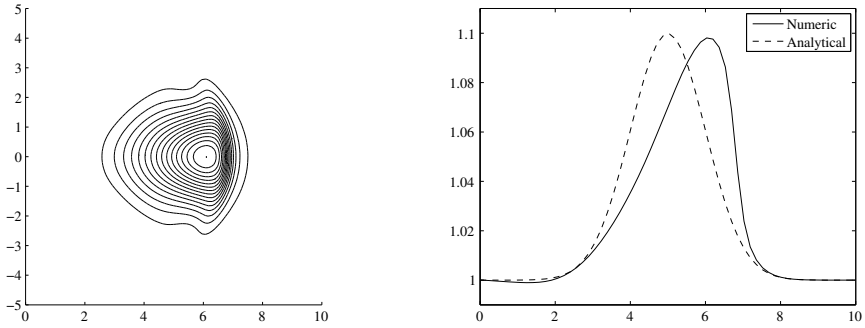

(d) $A = 10^{-1}$

Figure 2: Equatorial Kelvin wave. Water-height contours and slice plots along the line $y = 0$ for four different amplitudes, obtained by the STLDA scheme.

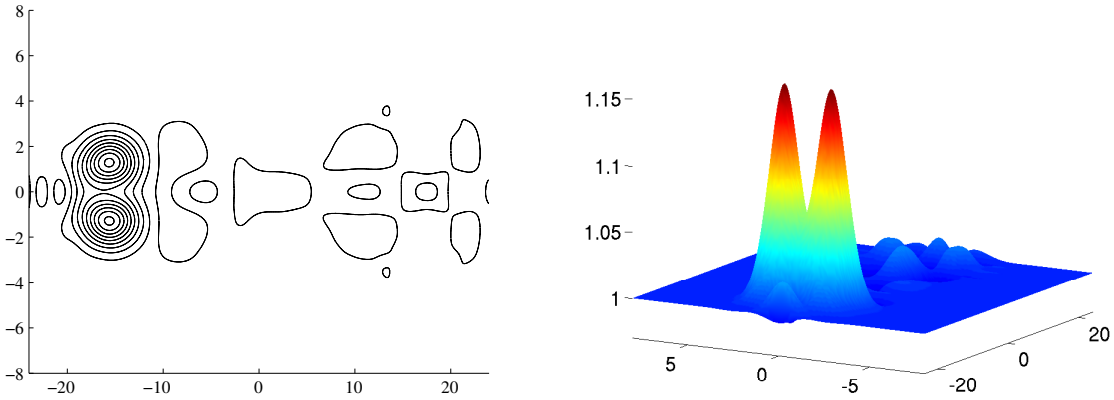

(a) STLDA: $d_{\max} = 1.165$ at $(x, y) = (-15.66, 1.30)$

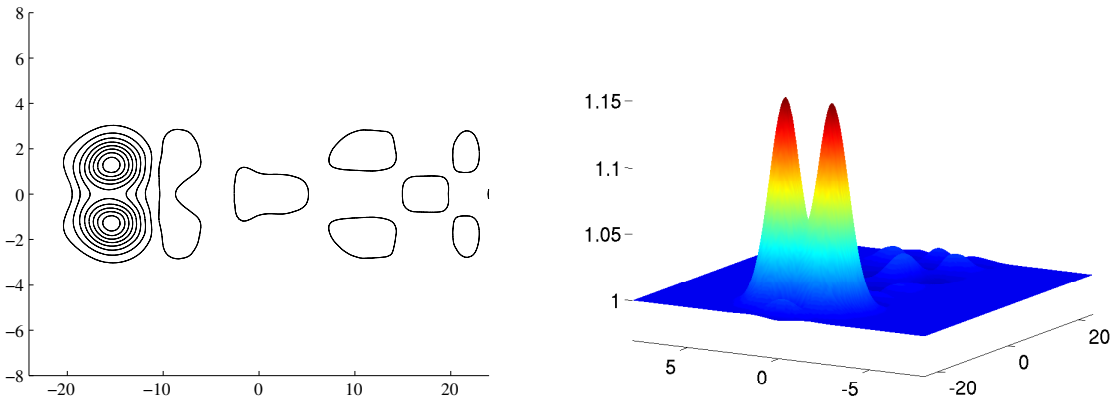

(b) STB: $d_{\max} = 1.156$ at $(x, y) = (-15.34, -1.25)$

Figure 3: Equatorial Rossby soliton. Contours and three-dimensional plots of the level of free surface for the STLDA (top) and STB (bottom) schemes.

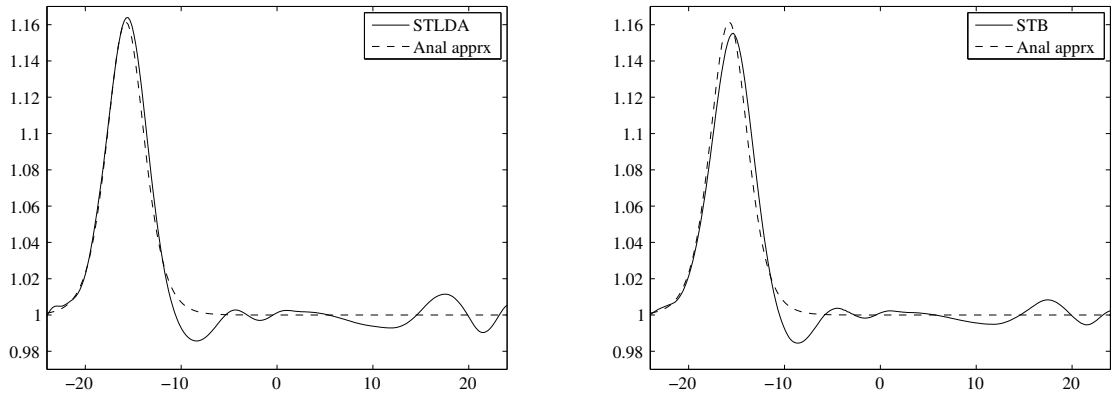

(a) Slice plot along the line $y = 1.23$ for the STLDA and STB schemes

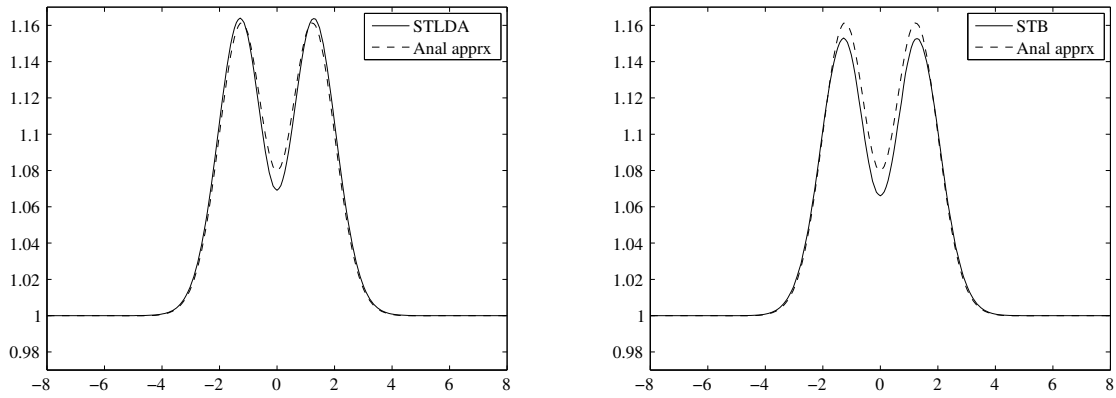

(b) Slice plot along the line $x = -15.77$ for the STLDA and STB schemes

Figure 4: Equatorial Rossby soliton. Free-surface slice plots along two, perpendicular, lines the STLDA and STB schemes.

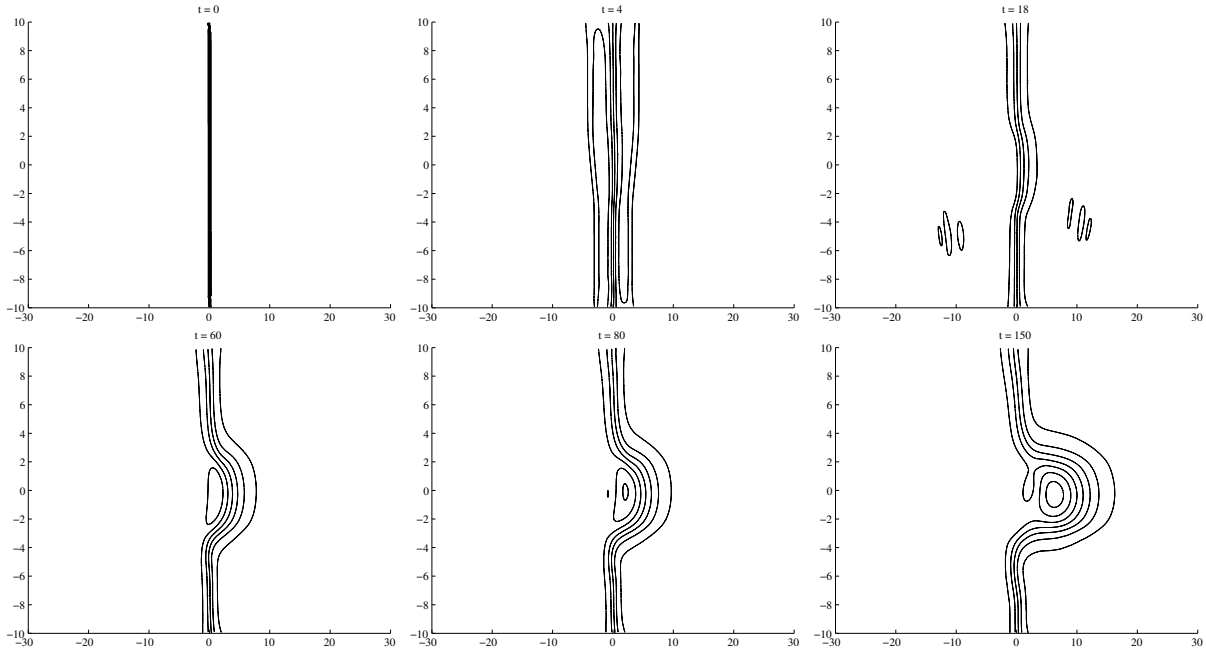

Figure 5: Nonlinear front adjustment. Eleven equidistant contours between 0.95 and 1.15 obtained by the STB scheme.

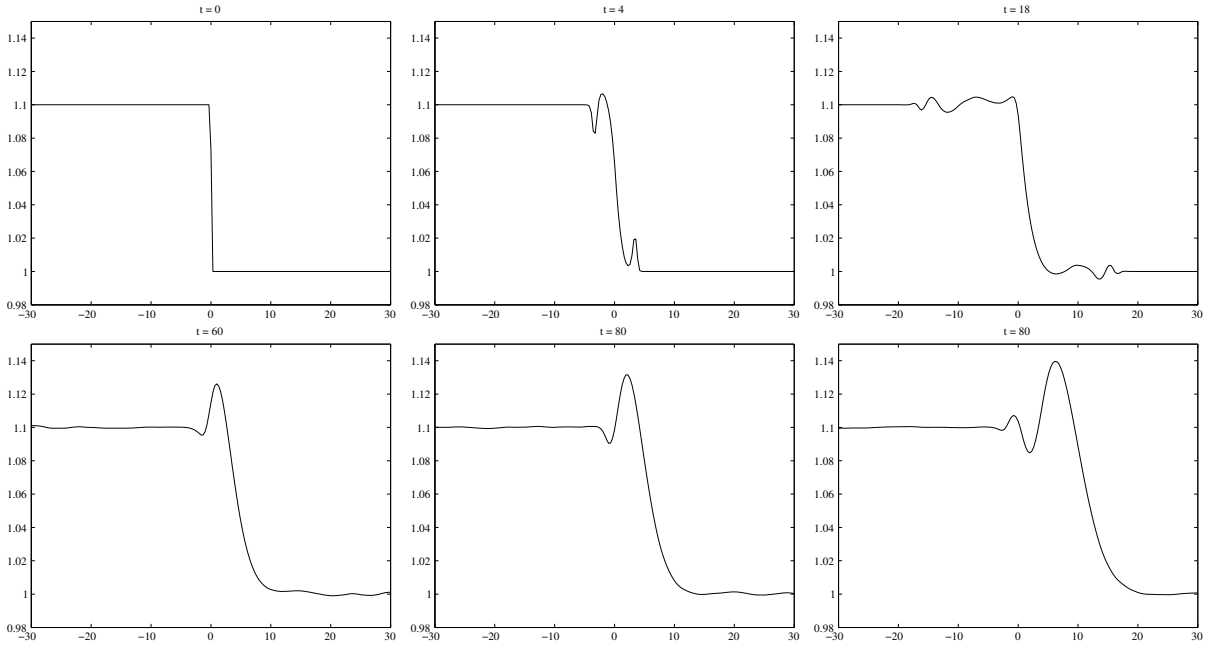

Figure 6: Nonlinear front adjustment. Slice plots of the free surface along the line $y = 0$ obtained by the STB scheme.

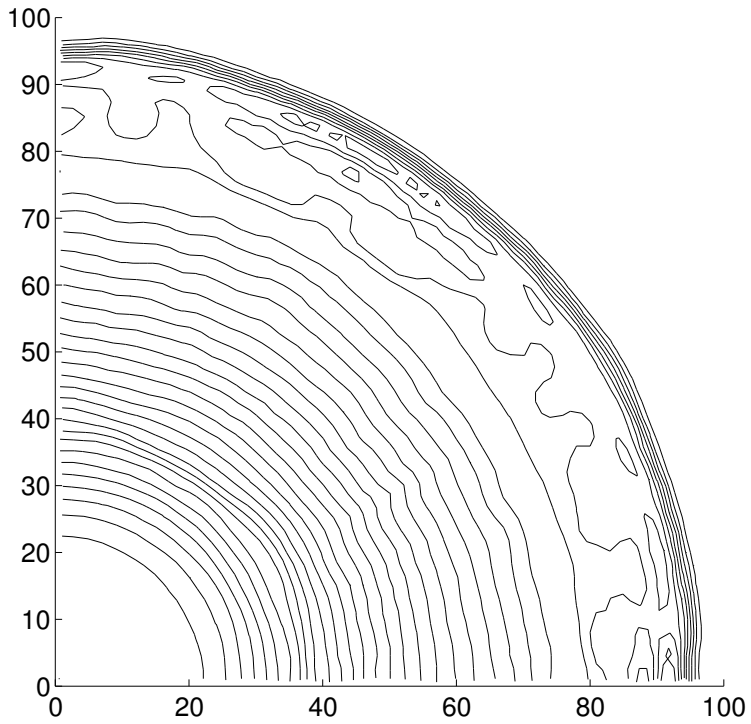

Figure 7: Nonlinear Stommel problem. The contours – obtained by the STLDA scheme – depict the water-height anomaly compared with the level of the still, current-free ocean.